JOURNAL OF THERMOPHYSICS AND HEAT TRANSFER
Vol. 19, No. 3, July–September 2005

Combustion of Moving Droplets and Suspended Droplets: Transient Numerical Results

Daniel N. Pope,* Damon Howard,† Kun Lu,‡ and George Gogos§
University of Nebraska at Lincoln, Lincoln, Nebraska 68588-0656

A numerical investigation of unsteady liquid fuel droplet combustion within an airstream at atmospheric pressure and under zero-gravity condition is presented. Combustion is modeled using one-step finite rate kinetics. A new multicomponent formulation (appropriate for the finite volume method) is used to describe mass diffusion in the gas-phase accurately. Results obtained for both suspended droplets (constant relative velocity) and for moving droplets shown that the flame configurations are a function of the time histories of both the Reynolds number and the Damköhler number. For a moving droplet, the Reynolds number decreases with time (due to both relative velocity and droplet size reduction), but the Damköhler number increases with time. For a suspended droplet, both the Reynolds number and the Damköhler number decrease with time due to the droplet size reduction. Consequently, for the same initial Reynolds number, suspended droplets may demonstrate different burning behavior than moving droplets. Within the range of initial Reynolds numbers considered (6, 8, and 50), a moving droplet tends to develop an envelope flame at some stage during its lifetime, whereas a suspended droplet develops an envelope flame only for low initial Reynolds numbers. The flame configurations present during droplet burning are critical in determining droplet lifetime.

Nomenclature

A = preexponential factor
a = fuel concentration exponent in reaction rate equation
b = oxygen concentration exponent in reaction rate equation
C_D = drag coefficient
c_p = specific heat capacity at constant pressure
Da = Damköhler number, Eq. (12)
D_{ij} = binary diffusion coefficient for the i–j pair
D_{im} = effective diffusion coefficient for the ith species
$D_{T,i}$ = thermal diffusion coefficient for the ith species
d = droplet diameter
E_a = activation energy
F_F = friction drag force
F_P = pressure drag force
F_T = thrust drag force
H_1 = downstream flame dimension
H_2 = upstream flame dimension
h = specific enthalpy
K = evaporation constant
k = thermal conductivity
L = latent heat of vaporization
$\dot{m}''_\theta$ = local mass flux at droplet surface
N = total number of chemical species
n_r = number of radial grid points
n_θ = number of tangential grid points
p = pressure
R = droplet radius
Re = Reynolds number, Eq. (11)
R_u = universal gas constant
r = radial position
T = temperature
T_0 = initial droplet temperature
t = time
t_d = droplet lifetime
U_∞ = freestream velocity
$\boldsymbol{V}_i$ = diffusion velocity of the ith species
$\boldsymbol{v}$ = velocity vector
v_r = velocity component in radial direction
v_θ = velocity component in polar direction
W = one-half of the lateral flame dimension
W_i = molecular weight of ith species
$\boldsymbol{W}_i$ = component of $\boldsymbol{V}_i$ caused by temperature gradient
X_i = mole fraction of ith species
Y_i = mass fraction of ith species
Δr = radial grid spacing
$\delta \boldsymbol{V}_i$ = correction velocity for $\boldsymbol{V}_i$
μ = dynamic viscosity
ν = kinematic viscosity
ν''_i, ν'_i = stoichiometric coefficient of the ith product and reactant, respectively
θ = polar position
ρ = density
$\bar{\rho}$ = average density
τ_{rr}, $\tau_{r\theta}$ = shear-stress tensor components
ω_i = rate of mass production of the ith species per unit volume

Subscripts

f = fuel or flame
g = gas phase
i = ith species
l = liquid phase
o = oxygen (O_2)
s = droplet surface
0 = initial condition
∞ = freestream or outer computational boundary

Received 6 August 2004; revision received 15 October 2004; accepted for publication 18 October 2004.

[*] Research Assistant Professor, Department of Mechanical Engineering, N104 Walter Scott Engineering Center; currently Assistant Professor, University of Minnesota Duluth, Department of Mechanical and Industrial Engineering, 105 VKH, 1305 Ordean Court, Duluth, MN 55812-3042.

[†] Graduate Student, Department of Mechanical Engineering, N104 Walter Scott Engineering Center.

[‡] Graduate Student, Department of Mechanical Engineering, N104 Walter Scott Engineering Center.

[§] Associate Professor, Department of Mechanical Engineering, N104 Walter Scott Engineering Center; ggogos@unl.edu.

Superscripts

T = transpose
$*$ = dimensionless variable

I. Introduction

EXPERIMENTAL studies to determine the burning characteristics of droplets under forced convection employ either porous spheres or suspended droplets. In both types of experiments, the ambient oxidizer is often blown over the "droplet" at a set velocity (freestream velocity). Porous sphere experiments, such as those conducted by Spalding[1] and Gollahalli and Brzustowski[2] under normal-gravity conditions, showed that the freestream velocity could be changed so that the resulting flame, formed in the wake of the droplet (wake flame), partially surrounded the droplet (transition flame), or completely enveloped the droplet (envelope flame). The microgravity suspended droplet combustion experiments of Okajima and Kumagai[3] utilized a constant freestream velocity to investigate the variation of the droplet diameter and flame dimensions over the droplet lifetime. Suspended droplet experiments[3–5] using a constant freestream velocity are more closely related (than porous sphere experiments) to the moving droplet present in a combustion chamber because they include transient effects such as droplet heat up, variations in the flame dimensions, and the decrease in droplet diameter due to evaporation. Dwyer and Sanders[6] were one of the first research teams to develop an unsteady numerical model for the moving droplet case. They predicted a transition from a wake to an envelope flame as the droplet velocity decreased.

The present study addresses the difference in combustion behavior, given the same initial conditions, of an isolated liquid fuel droplet under two scenarios: moving droplet and suspended droplet combustion in a forced convection environment. The first problem simulates the injection of a droplet into a combustion chamber. In this case, the droplet is allowed to decelerate due to the drag force. The second scenario simulates the conditions that are typically present in experiments that employ the suspended droplet technique (constant velocity). A numerical model has been developed to simulate the two cases. The equations and methods employed in our model, the validation of the model, and results for n–heptane droplet combustion are presented hereafter.

II. Theoretical Formulation

The problem considered is that of a single-component (n–heptane) liquid fuel droplet undergoing evaporation and combustion in a hot, convective, low-pressure, zero-gravity environment of infinite expanse (Fig. 1). The freestream pressure p_∞ and freestream temperature T_∞ are constant. For a moving droplet, the relative velocity U_∞ between the droplet and freestream is subject to change due to the influence of the drag force on the droplet. For a suspended droplet, the relative velocity is constant. The remaining assumptions employed in the model include the following: 1) The flow is axisymmetric and laminar. 2) The droplet maintains a spherical shape. 3) The effect of the fiber in the suspended droplet case is negligible. 4) Thermal radiation is negligible. 5) The Dufour effect and pressure diffusion are negligible. 6) Viscous dissipation and pressure work are negligible. 7) Solubility of gas-phase species into the liquid phase is negligible.

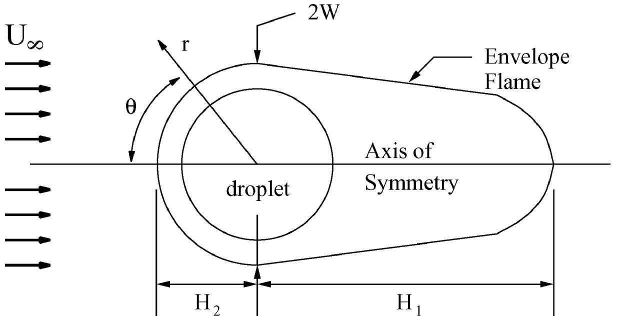

Fig. 1 Problem schematic and envelope flame dimensions.

The governing equations for the gas phase and the liquid phase consist of the unsteady, axisymmetric equations of mass, momentum, species (gas phase only), and energy conservation with variable properties.[7] The conservation of mass and momentum equations in the gas phase and the liquid phase are given by

$$\frac{\partial \rho}{\partial t} + \nabla \cdot (\rho \boldsymbol{v}) = 0$$

$$\frac{\partial}{\partial t}(\rho \boldsymbol{v}) + \nabla \cdot (\rho \boldsymbol{v}\boldsymbol{v}) = -\nabla p - \nabla\left[\frac{2}{3}\mu(\nabla \cdot \boldsymbol{v})\right] + \nabla \cdot \{\mu[(\nabla \boldsymbol{v}) + (\nabla \boldsymbol{v})^T]\} - \rho\frac{\mathrm{d}\boldsymbol{U}_\infty}{\mathrm{d}t}$$

where $\mathrm{d}\boldsymbol{U}_\infty/\mathrm{d}t$ is the acceleration of the coordinate system and the superscript T denotes the transpose of the tensor. Conservation of energy in the gas phase is described by

$$\frac{\partial}{\partial t}(\rho T) + \nabla \cdot (\rho \boldsymbol{v} T) = \nabla \cdot \left(\frac{k}{c_p}\nabla T\right) + \frac{k}{c_p^2}\nabla T \cdot \nabla c_p - \frac{1}{c_p}\sum_{i=1}^{N}\rho Y_i \boldsymbol{V}_i \cdot \nabla h_i - \frac{1}{c_p}\sum_{i=1}^{N}\omega_i h_i$$

The last two terms in the right-hand side of the preceding equation are not present in the liquid-phase conservation of energy equation.

In addition to the preceding equations, the species diffusion velocities $\boldsymbol{V}_i$ are calculated using the following:

$$\nabla X_i = \sum_{j=1}^{N}\left(\frac{X_i X_j}{D_{ij}}\right)(\boldsymbol{V}_j - \boldsymbol{V}_i) + \sum_{j=1}^{N}\left[\left(\frac{X_i X_j}{\rho D_{ij}}\right)\left(\frac{D_{T,j}}{Y_j} - \frac{D_{T,i}}{Y_i}\right)\right]\left(\frac{\nabla T}{T}\right) \tag{1}$$

for $i = 1, \ldots, N$, where N is the number of species. The N equations for the diffusion velocities are subject to the constraint

$$\sum Y_i \boldsymbol{V}_i = 0$$

and the thermal diffusion coefficients have the following property.[8]

$$\sum D_{T,i} = 0$$

In the current model, the diffusion velocity is defined as

$$\boldsymbol{V}_i = -(D_{im}/Y_i)\nabla Y_i + \delta \boldsymbol{V}_i + \boldsymbol{W}_i$$

where

$$\boldsymbol{W}_i = -(D_{T,i}/\rho Y_i)(\nabla T/T)$$

is the thermal diffusion velocity and

$$D_{im} = \frac{1 - X_i}{\sum_{j \neq i}(X_j/D_{ij})}$$

is the effective diffusion coefficient for the ith species into the mixture of all other species. (See, for example, Ref. 8 and method V in Ref. 9.) Here, $\delta \boldsymbol{V}_i$ is a correction velocity to satisfy equation (1). Using the identities

$$\sum Y_i = 1, \qquad X_i = \frac{(Y_i/W_i)}{\sum(Y_j/W_j)}$$

in the preceding equations and rearranging gives an expression for the correction velocities

$$\delta \boldsymbol{V}_i \sum_{j\neq i} \frac{Y_j}{W_j D_{ij}} - \sum_{j\neq i} \frac{Y_j}{W_j D_{ij}} \delta \boldsymbol{V}_j = \sum_{j\neq i} \frac{1}{W_j}\left(1 - \frac{D_{jm}}{D_{ij}}\right)\nabla Y_j \tag{2}$$

for $i = 1, \ldots, N$, which are subject to the constraint

$$\delta \boldsymbol{V}_i + \sum_{j\neq i} Y_j \delta \boldsymbol{V}_j = \sum_{j=1}^{N} D_{jm}\nabla Y_j + \delta \boldsymbol{V}_i (1 - Y_i) \tag{3}$$

The resulting gas-phase conservation of species equation, which is appropriate for use with the finite volume method, is

$$\frac{\partial}{\partial t}(\rho Y_i) + \nabla \cdot [\rho(\boldsymbol{v} + \delta \boldsymbol{V}_i + \boldsymbol{W}_i) Y_i] = \omega_i + \nabla \cdot (\rho D_{im} \nabla Y_i)$$

The gas- and liquid-phase governing equations are coupled at the interface by the following equations, which are shown in spherical coordinates: Continuity of the tangential velocity is

$$v_{\theta,g,s} = v_{\theta,l,s} \tag{4}$$

Continuity of the shear stress is

$$\mu_{g,s}\left[\frac{\partial v_\theta}{\partial r} - \frac{v_\theta}{r} + \frac{1}{r}\frac{\partial v_r}{\partial \theta}\right]_{g,s} = \mu_{l,s}\left[\frac{\partial v_\theta}{\partial r} - \frac{v_\theta}{r} + \frac{1}{r}\frac{\partial v_r}{\partial \theta}\right]_{l,s} \tag{5}$$

Continuity of the temperature is

$$T_{g,s} = T_{l,s} \tag{6}$$

Conservation of species is, for fuel

$$\dot{m}''_\theta = \dot{m}''_\theta Y_{f,s} + \rho_{g,s} Y_{f,s} V_{r,f,s} \tag{7}$$

and for nonfuel

$$0 = \dot{m}''_\theta Y_{i,s} + \rho_{g,s} Y_{i,s} V_{r,i,s} \tag{8}$$

Conservation of energy is

$$\dot{m}''_\theta L = k\frac{\partial T}{\partial r}\bigg|_{g,s} - k\frac{\partial T}{\partial r}\bigg|_{l,s} \tag{9}$$

Conservation of mass is

$$\dot{m}''_\theta = \rho_{g,s}\left(v_{r,g,s} - \frac{\mathrm{d}R}{\mathrm{d}t}\right) = \rho_{l,s}\left(v_{r,l,s} - \frac{\mathrm{d}R}{\mathrm{d}t}\right) \tag{10}$$

Phase equilibrium, through the use of Wagner's equation (see Ref. 10) is employed to calculate the partial pressure of the gaseous fuel at the droplet surface.

The axisymmetric governing equations are solved in spherical coordinates ($r - \theta$). The origin of the coordinate system is the droplet center. The computational boundary is located at r_∞ and consists of two regions in the gas phase: the inflow region ($0 \leq \theta \leq \pi/2$) where the values for all dependent variables are specified and the outflow region ($\pi/2 < \theta \leq \pi$) where a zero gradient normal to the boundary is assumed. The polar velocity v_θ is zero along the axis of symmetry, and a zero gradient normal to this boundary is assumed for all other variables. The initial conditions are as follows: a uniform initial droplet temperature T_0, the pressure equal to p_∞ everywhere, velocities set to zero everywhere, and the gas-phase temperature and composition set to their freestream values. Initial conditions for the temperature and composition at the liquid/gas interface are determined via the solution of the interface equations.

The surface regression rate ($\mathrm{d}R/\mathrm{d}t$) is calculated using overall conservation of mass for the droplet:

$$\frac{\mathrm{d}R}{\mathrm{d}t} = -\frac{1}{2\bar{\rho}_l}\left(\int_0^\pi \dot{m}''_\theta \sin\theta \, \mathrm{d}\theta + \frac{2}{3}R\frac{\mathrm{d}\bar{\rho}_l}{\mathrm{d}t}\right)$$

For the suspended droplet (stationary), the $r - \theta$ coordinate system is inertial, whereas for the moving droplet, the coordinate system is noninertial. The effect of the acceleration of the noninertial coordinate system ($\mathrm{d}\boldsymbol{U}_\infty/\mathrm{d}t$) is included in the momentum equations. Overall conservation of momentum for the droplet, which is given by

$$\frac{\mathrm{d}U_\infty}{\mathrm{d}t} = -\frac{3}{8}C_D\frac{U_\infty^2}{R}\left(\frac{\rho_\infty}{\bar{\rho}_l}\right) - \frac{3}{2}\frac{1}{R^3\bar{\rho}_l}\frac{\mathrm{d}}{\mathrm{d}t} \times \left[\int_0^\pi\int_0^R \rho_l (v_{r,l}\cos\theta - v_{\theta,l}\sin\theta) r^2 \sin\theta \, \mathrm{d}r \, \mathrm{d}\theta\right]$$

is used to calculate the droplet acceleration, where $\bar{\rho}_l$ is the average liquid-phase density and the subscript l indicates values in the liquid phase. For completeness, the definition of C_D in terms of the friction F_F, pressure F_P, and thrust F_T force is also given here:

$$C_D = \frac{2(F_P + F_F + F_T)}{\rho_\infty U_\infty^2 \pi R^2}$$

$$F_F = 2\pi R^2 \int_0^\pi (\tau_{r\theta,g}\sin\theta - \tau_{rr,g}\cos\theta)_s \sin\theta \, \mathrm{d}\theta$$

$$F_P = 2\pi R^2 \int_0^\pi p_{g,s}\cos\theta\sin\theta \, \mathrm{d}\theta$$

$$F_T = 2\pi R^2 \int_0^\pi \dot{m}''_\theta (v_{r,g}\cos\theta - v_{\theta,g}\sin\theta)_s \sin\theta \, \mathrm{d}\theta$$

where the subscripts g and s denote evaluation in the gas phase and at the droplet surface, respectively.

Variable properties in the gas phase were calculated using the ideal gas law and low-pressure correlations from Reid et al.[10] Species viscosities and thermal conductivities were calculated using the method of Chung et al.[11] (See also Ref. 10.) Mixture viscosity and thermal conductivity were obtained using the method of Wilke.[12] (See also Ref. 10.) The curve fits of McBride et al.[13] were used to calculate the specific heat capacities and enthalpies. Binary diffusion coefficients were evaluated using the first approximation from kinetic theory[10,14] and the Lennard–Jones 12-6 potential. An approximation developed by Ramshaw[15] was used to calculate the thermal diffusion coefficients. The properties of n–heptane in the liquid phase were calculated employing the correlations used by Haywood et al.[16]

A one-step overall reaction is used to model the combustion of n–heptane in dry air:

$$\mathrm{C_7H_{16}} + 11(\mathrm{O_2} + 3.77\mathrm{N_2}) \rightarrow 7\mathrm{CO_2} + 8\mathrm{H_2O} + 11(3.77\mathrm{N_2})$$

The resulting expression for ω_i is

$$\omega_i = W_i(\nu''_i - \nu'_i)A(\rho Y_f/W_f)^a(\rho Y_o/W_o)^b \exp[-E_a/R_u T]$$

where the subscripts f and o indicate fuel and oxygen. The preexponential factor A, the activation energy E_a, and the fuel and oxygen concentration exponents a and b for a one-step overall reaction were determined empirically using a quasi-steady version of the current code.[17] The reaction was assumed to be first order with respect to fuel and oxygen ($a = b = 1$). Appropriate values for A and E_a were determined by matching numerical results for extinction velocity to experimental data available in the literature. The resulting kinetics parameters are given in Table 1. These parameters are used in the present work.

Table 1 Reaction rate parameters used for the present study[17]

Parameter	Value
A, m^3/kmol · s	3.35×10^{11}
E_a, kJ/kmol	1.53×10^5
a	1.0
b	1.0

Table 2 Computational grids

Initial Reynolds number	$\Delta r^*_{s,0}$	r^*_∞	n_θ	$n_{r,g}$	$n_{r,l}$
100	0.02	30	90	100	25
1–50	0.025	50	90	150	25
0.01	0.025	125	60	250	25

III. Numerical Model

The governing equations are discretized using the finite volume[18] and SIMPLEC[19] methods. Convection–diffusion is modeled using the power-law scheme.[18] A collocated grid[20] is adopted. The discretization equations, with the exception of Eqs. (2) and (3), are solved using the alternating direction implicit method with the tridiagonal matrix algorithm used on each line of the two alternating directions. The N δV_i defined by Eqs. (2) and (3) are calculated at each grid point using Gauss–Seidel iteration. Equation (3) is used for the δV_i that corresponds to the species with the maximum Y_i. The iterative solution of the governing equations is performed within each time step until convergence is achieved. The calculations are terminated when the droplet radius is less than 1/10 of its initial value ($R < 0.1 R_0$).

The computational grid consists of adjoining orthogonal control volumes with uniform tangential grid spacing and nonuniform radial grid spacing. In the radial direction, hyperbolic tangent stretching functions[21] are used to concentrate grid points near the droplet surface in both the gas phase and liquid phase. The nonuniform radial grid extends from the instantaneous droplet radius R to a fixed computational boundary r_∞ in the gas phase and from the droplet center to R in the liquid phase. The following parameters define the grid spacing: the initial dimensionless spacing next to the droplet surface ($\Delta r^*_{s,0} = \Delta r_{s,0}/R_0$), the dimensionless location of the computational boundary r^*_∞, the number of tangential grid points n_θ, and the number of radial grid points in the gas phase $n_{r,g}$ and liquid phase $n_{r,l}$. Because of the nature of the problem under investigation and the range of initial Reynolds numbers Re_0 employed in the present work, the three different computational grids shown in Table 2 were used in the numerical solutions.

The numerical model's accuracy and sensitivity to grid size and spacing were initially tested by isolating pertinent sections of the code and comparing predicted results to available numerical and experimental correlations. Predicted drag coefficients for isothermal spheres with Reynolds numbers between 0.01 and 100 were within 2% of the correlations of Clift et al.[22] Nusselt numbers for constant property flow past a solid sphere were within 1% of the numerical results of Sayegh and Gauvin.[23] For flow past an isothermal sphere of water at Reynolds numbers of 30 and 100, the predicted drag coefficients were within 2% of the numerical calculations of LeClair et al.[24] The assembled code was also tested via comparison of numerical results for a solid sphere of n–heptane evaporating in air at 800 K to the drag[25] and Nusselt number correlations of Renksizbulut and Yuen.[26] For Reynolds numbers from 15 to 100, the current code predicts drag coefficients that are from 7 to 8% lower than the correlation, and Nusselt numbers that are from 8% lower to 4% higher than the correlation. Further refinement of the grid size or enlarging the r^*_∞ shown in Table 2 changed the predicted values by less than 0.2%.

The grid spacing and time step used in the droplet combustion simulations were tested to ensure that all solutions are reasonably independent of these parameters. Simulations covering one-quarter of the droplet lifetime were conducted with 50% more radial or tangential grid points, one-half $\Delta r^*_{s,0}$, or one-half of the time step used to generate the final results. The accumulated difference in flame dimensions was less than 2%, and values at the droplet surface, such as the instantaneous radius and drag coefficient, differed by less than 0.1%.

The fuel vapor/air mixture that surrounds the droplet can undergo two types of ignition. Ignition may be caused by either a high ambient temperature or the presence of an external ignition source. In the former case, the code is run as is, and ignition occurs if the ambient temperature is sufficiently high. In the latter case, the code is run for a few time steps so that a fuel vapor/air mixture builds up around the droplet. Energy is then added to an axisymmetric region upstream of the droplet via the source term in the conservation of energy equation. The addition of energy occurs over several time steps and is terminated when ignition takes place. Thus, a minimum amount of energy is introduced to cause ignition.

IV. Model Validation

The accurate modeling of the change in droplet velocity due to the drag force is required for the moving droplet case. As part of the validation procedure, combustion was disabled, and the transient code was tested via comparison to numerical results for the evaporation of a moving droplet. Haywood et al.[16] present results for an n–heptane droplet with $T_0 = 298$ K and an initial Reynolds number Re_0 of 100 that is evaporating in air at 800 K and 1 atm. Figure 2 shows their results (dash–dot line) for dimensionless radius ($R^* = R/R_0$), dimensionless droplet velocity ($U^*_\infty = U_\infty/U_{\infty,0}$), and the ratio of the instantaneous to the initial Reynolds number (Re/Re_0) vs dimensionless time ($t^* = tU_{\infty,0}/R_0$). Results from the current code (solid lines) are in excellent agreement. The maximum accumulated differences between the current results and those of Haywood et al.[16] are less than 0.2% for R^* and less than 7% for U^*_∞ and Reynolds number. The difference in predicted velocity and Reynolds number is caused by an approximately 8% difference in the predicted drag coefficient (not shown).

Experimental data available in the literature[3,4,27] for microgravity droplet combustion have been used to validate the transient code. Kumagai et al.[27] studied the spherically symmetric combustion of free n–heptane droplets in air at atmospheric conditions. A drop tower was used to generate microgravity conditions. Air at atmospheric conditions was numerically modeled using $T_\infty = 300$ K and $p_\infty = 1$ atm. In the experiments, a spark was applied near the droplet to cause ignition. Droplet ignition was accomplished numerically through the use of the energy addition discussed earlier. Spherically symmetric combustion was modeled using a constant freestream velocity that corresponded to an initial Reynolds number of 0.01. The initial droplet temperature was assumed to be 298 K. Figure 3 shows results for the dimensionless diameter squared $(d/d_0)^2$ and flame diameter d_f vs time after ignition for an n–heptane droplet with an initial diameter d_0 of 0.98 mm. For the numerical results

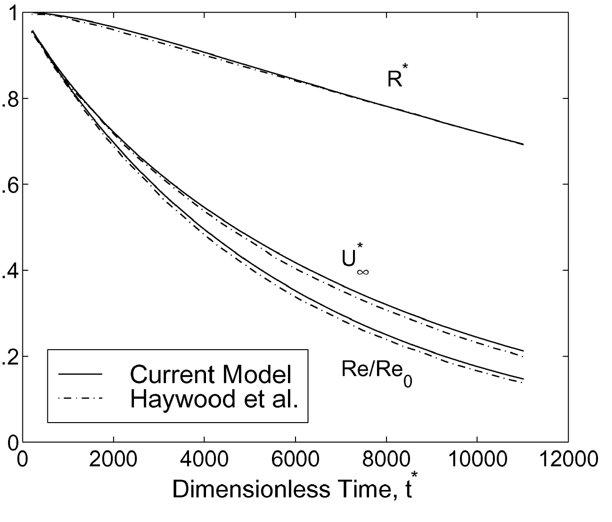

Fig. 2 **Time history of R^*, U^*_∞, and Re/Re_0 for n–heptane droplet with $Re_0 = 100$ evaporating in air at 800 K and 1 atm.**

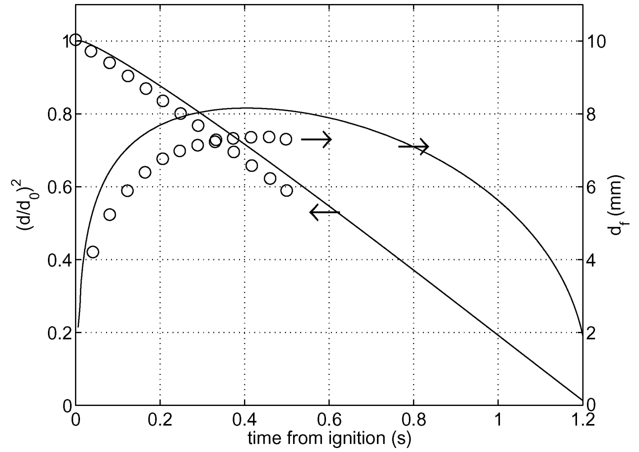

Fig. 3 Time history of $(d/d_0)^2$ and d_f for spherically symmetric n–heptane droplet combustion in air ($d_0 = 0.98$ mm): ○, experimental atmospheric conditions and microgravity[27] and ——, numerical, $Re_0 = 0.01$, $T_\infty = 300$ K, $p_\infty = 1$ atm, and zero gravity.

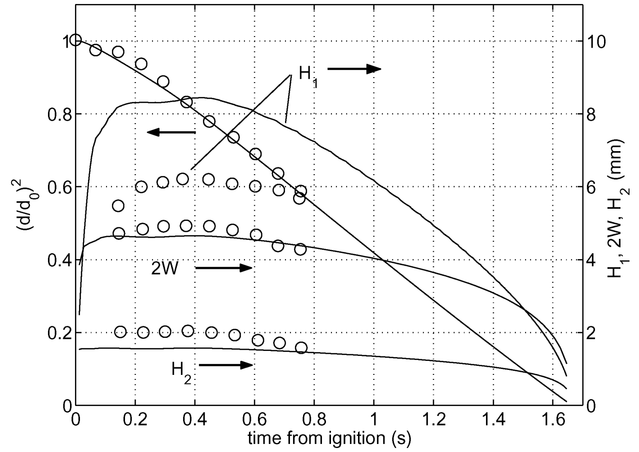

Fig. 4 Time history of $(d/d_0)^2$ and flame dimensions for suspended n–heptane droplet combustion in air with constant freestream velocity $U_\infty = 19.9$ cm/s and $d_0^2 = 1.5$ mm²: ○, experimental, atmospheric conditions and microgravity[3] and ——, numerical, $T_\infty = 300$ K, $p_\infty = 1$ atm, and zero gravity.

(solid lines), time zero corresponds to the start of the energy addition. There is good agreement in d^2 dependence between the current numerical results (lines) and the experimental results (circles). The numerical results for d_f are approximately 15% higher than the experimental data. The flame diameter is defined numerically as the location of maximum temperature, and the plot starts when the flame completely envelops the droplet. Both the experimental data and the numerical results show that d_f reaches its maximum value between 0.4 and 0.5 s from ignition. The numerical prediction for the ratio d_f/d (not shown) increases during the life of the droplet. The evaporation constant (not shown) increases rapidly as the droplet ignites and reaches a value of about 0.8 mm²/s at approximately one-third ($t = 0.4$ s) of the droplet lifetime. Kumagai et al.[27] reported an evaporation constant of 0.78 mm²/s. An evaporation constant of 0.8 mm²/s was measured by Nayagam et al.[4] for spherically symmetric n–heptane droplet combustion.

Results from our numerical simulations and microgravity experimental data under forced convection (see Ref. 3) were also in good agreement. Okajima and Kumagai[3] gave data for d^2 and flame dimensions vs time from ignition for a suspended n–heptane droplet with $d_0^2 = 1.5$ mm² and a constant freestream velocity U_∞ of 19.9 cm/s. Their experiments were conducted using air at atmospheric conditions, and a spark was used to ignite the droplet. Figure 4 shows results for $(d/d_0)^2$ and the upstream H_2, lateral $2W$, and downstream H_1 flame dimensions (Fig. 1). Our simulations of this case (solid lines) showed excellent agreement with the experimental data (circles) for $(d/d_0)^2$, H_2, and $2W$. The predicted downstream flame dimension H_1 was approximately 30% higher than the experimental result. In the experiment, the droplet suspender was located in the wake of the droplet where the presence of soot was noted. The current code does not model the presence of the suspender, the formation of soot, and soot-induced radiation. The inclusion of soot, and its associated continuum radiation in the model would tend to increase the numerical result for H_1 (Refs. 28–30), whereas including the droplet suspender in the model would tend to decrease the numerical result for H_1 (Ref. 27). Based on the difference between the experimental and numerical value for H_1, it appears the droplet suspender has a greater effect on H_1.

V. Results and Discussion

The numerical model was used to investigate the combustion of an n–heptane droplet with an initial diameter of 500 μm. Two cases were studied: 1) a moving droplet and 2) a suspended droplet within a convective environment. The results presented here are for $T_\infty = 1200$ K, $p_\infty = 1$ atm, $T_0 = 298$ K, and initial Reynolds numbers of 6, 8, and 50. The numerical simulations for all of these cases do not include an external ignition source.

Table 3 compares the lifetimes of both moving and suspended n–heptane droplets for the Reynolds numbers considered. Table 3 contains interesting results that require explanation. For example, the lifetime of a moving droplet with $Re_0 = 50$ is longer than the lifetimes of moving droplets with initial Reynolds numbers of 6 and 8. Furthermore, for the same initial Reynolds number, the suspended droplet burns out faster than its moving droplet counterpart in two cases ($Re_0 = 6$ and 50), whereas for $Re_0 = 8$, the result is the opposite. In the remainder of this section, the results presented in Table 3 will be discussed in detail.

Figure 5 shows the predicted temperature distribution at various times for a moving droplet with $Re_0 = 6$. The droplet initially

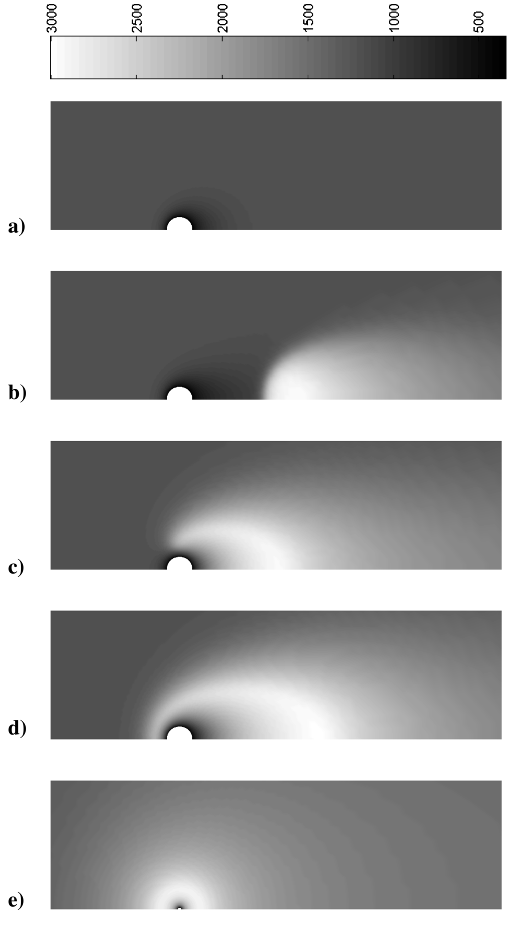

Fig. 5 Predicted gas-phase temperature distribution, in degrees Kelvin around a moving droplet with $Re_0 = 6$ ($d_0 = 500$ μm and $T_\infty = 1200$ K): a) $t = 0.5$ ms, b) $t = 5.2$ ms (wake flame), c) $t = 6.9$ ms (transition flame), d) $t = 8.8$ ms (envelope flame), and e) $t = 224.7$ ms (envelope flame).

experiences pure evaporation (Fig. 5a). The fuel vapor mixes with the ambient oxidizer, and ignition occurs downstream of the droplet, forming a wake flame (Fig. 5b). In this particular case, the flame rapidly approaches the droplet, partially surrounds the droplet in a transition flame configuration (Fig. 5c), and eventually surrounds the droplet in an envelope flame configuration (Fig. 5d). An envelope flame remains until the end of the droplet lifetime (Fig. 5e).

Figure 6 shows the time history of the dimensionless droplet diameter squared $(d/d_0)^2$, Reynolds number, Damköhler number, and evaporation constant K for a suspended (dashed lines) and a moving (solid lines) droplet with $Re_0 = 6$. The suspended and moving droplet developed envelope flames at approximately the same time ($t \simeq 10$ ms). When the droplet lifetimes are considered (210 and 226 ms), this happened at a very early stage. Once the envelope flame formed, it remained for both droplets until the end of their lifetimes. Thus, during most of the droplet lifetime, both the suspended and the moving droplet experience the same flame configuration. This implies that the two droplets will exhibit similar burning behavior and, thus, similar lifetimes. Figure 6a shows that to be true. The droplets in both cases have very similar diameter squared time histories.

Table 3 n–heptane droplet lifetimes for suspended and moving droplets: $p_\infty = 1$ atm, $T_\infty = 1200$ K, $T_0 = 298$ K, and $d_0 = 500$ μm

Initial Reynolds number	Droplet	t_d, ms
6	Suspended	210
	Moving	226
8	Suspended	300
	Moving	230
50	Suspended	181
	Moving	238

Figure 6b shows the time history of the instantaneous Reynolds number Re for a suspended and a moving droplet with $Re_0 = 6$. Both Reynolds numbers decrease monotonically with time; however, they decrease at different rates. The Reynolds number is defined as

$$Re = d(t)U_\infty(t)/\nu_\infty \tag{11}$$

where ν_∞ is the kinematic viscosity evaluated at ambient conditions, and $d(t)$ and $U_\infty(t)$ are the instantaneous droplet diameter and freestream velocity. The freestream velocity remains constant for the suspended droplet. As a result, the Reynolds number changes only with the droplet diameter. However, for the moving droplet, the droplet diameter decreases, and the droplet velocity decreases due to drag. Thus, the Reynolds number for the moving droplet decreases faster than that for the suspended droplet.

The higher Reynolds number associated with the suspended droplet implies a stronger convection. This results in a higher evaporation constant for the suspended droplet than for the moving droplet, as shown in Fig. 6d. The evaporation constant is given by

$$K = -\frac{\mathrm{d}}{\mathrm{d}t}[d(t)^2]$$

At the beginning of the droplet lifetime, the evaporation constants for the two cases are very close, and both increase rapidly due to the high-temperature environment. A difference between the evaporation constants appears at about 1/10 of the lifetime due to the difference in the convective strength for the two cases. At the relatively low initial Reynolds number of 6, the difference in the evaporation constants between the suspended droplet and the moving droplet remains fairly small during the entire droplet lifetime. As a result, the droplet lifetimes for the two cases are close.

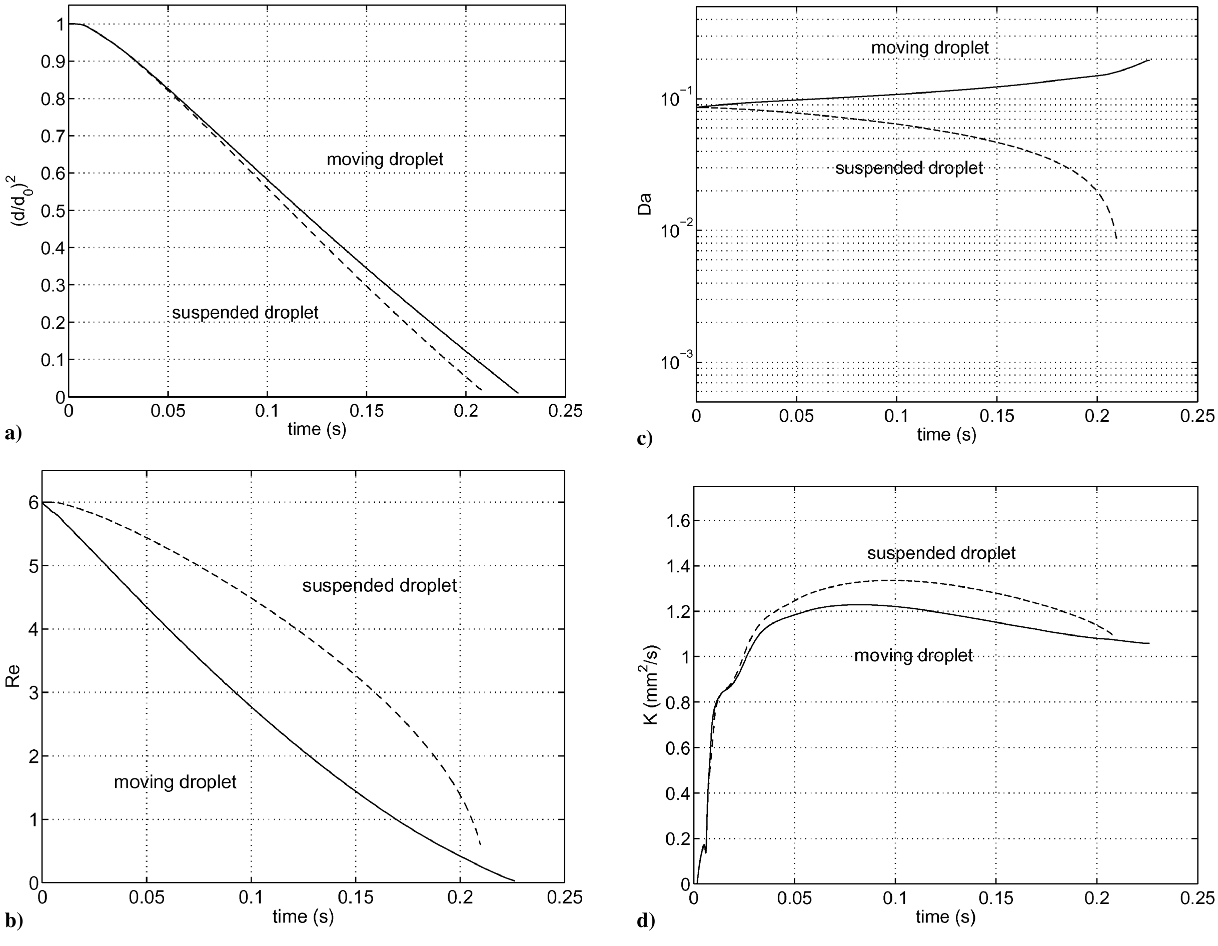

Fig. 6 Comparison between moving droplet and suspended droplet combustion for $Re_0 = 6$ ($d_0 = 500$ μm and $T_\infty = 1200$ K); time history of a) $(d/d_0)^2$, b) Reynolds number, c) Damköhler number, and d) K.

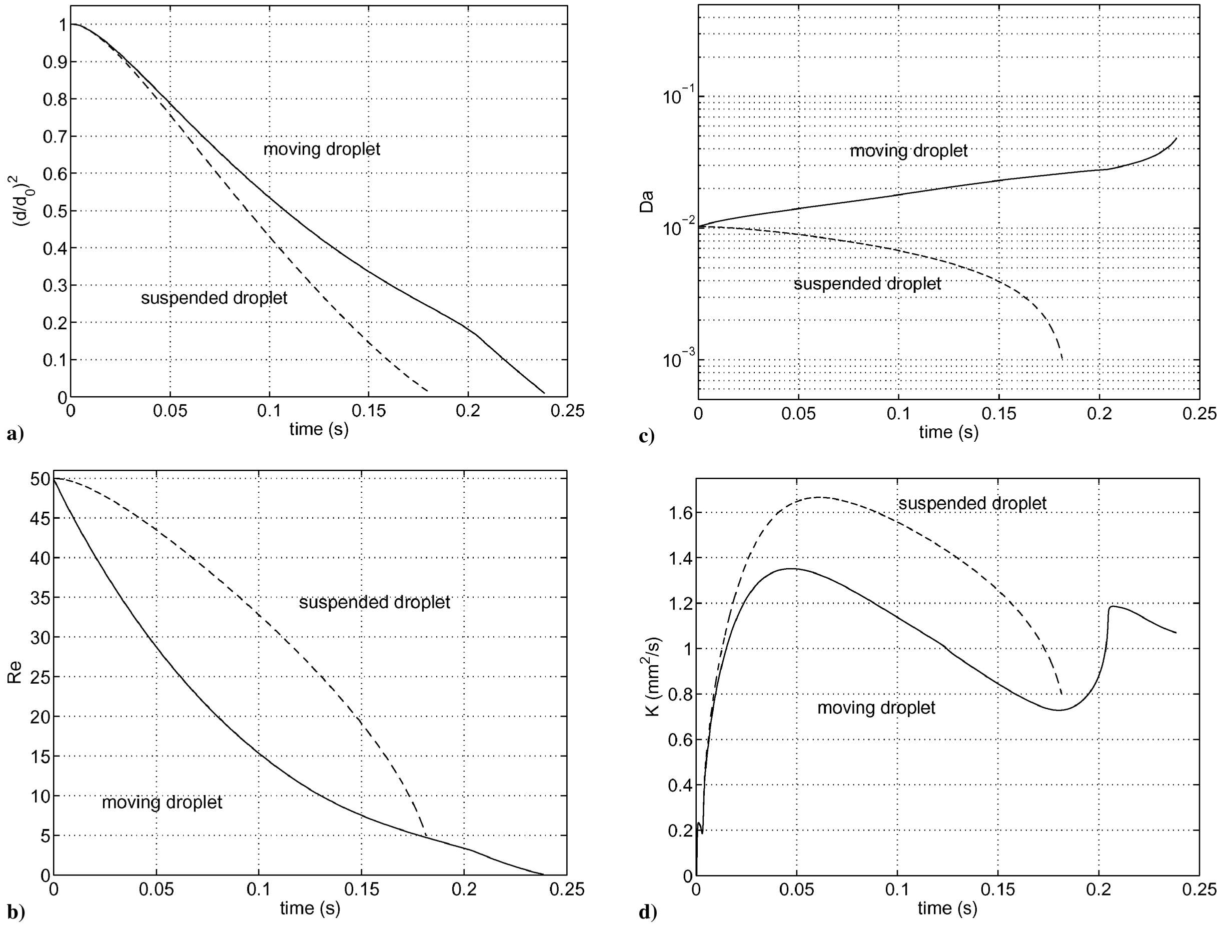

Fig. 7 Comparison between moving droplet and suspended droplet combustion for $Re_0 = 50$ ($d_0 = 500$ μm and $T_\infty = 1200$ K); time history of a) $(d/d_0)^2$, b) Reynolds number, c) Damköhler number, and d) K.

Figure 6c compares the instantaneous Damköhler numbers for a suspended and a moving droplet with $Re_0 = 6$. Here, the Damköhler number is defined as

$$Da = [R(t)/U_\infty(t)]A\rho_\infty^{a+b-1}W_f^{1-a}(1/W_o)^b \exp[-E_a/R_u T_\infty] \tag{12}$$

where W_o and W_f are molecular weights for the fuel and oxygen and $R(t)$ is the instantaneous droplet radius. The Damköhler number is proportional to the ratio of droplet diameter to instantaneous freestream velocity. This ratio is the characteristic convective time scale. Thus,

$$Da \propto \mathrm{d}(t)/U_\infty(t) = t_{\mathrm{conv}}$$

In Fig. 6c, the Damköhler number for the suspended droplet decreases with time, whereas for the moving droplet case it increases slowly with time. The former result is expected because, for the suspended case, U_∞ is constant whereas the droplet diameter decreases. This results in a monotonic decrease in Damköhler number. For the moving droplet case, both $d(t)$ and $U_\infty(t)$ decrease. The resulting trend in Damköhler number is not obvious. For $Re_0 = 6$, it seems that the droplet velocity decreases slightly faster than the droplet diameter.

Figure 7 shows the time history of $(d/d_0)^2$, Reynolds number, Damköhler number, and K for a suspended and a moving droplet with $Re_0 = 50$. With this higher initial Reynolds number, both droplets ignite in the wake areas far downstream. After ignition, for the moving droplet case, the flame moves toward the droplet and finally forms an envelope flame (at approximately $t = 205$ ms) near the end of its lifetime. For the suspended droplet, no envelope flame is developed throughout its lifetime, and the wake flame remains at approximately the same location for most of the droplet's lifetime.

The plots for $Re_0 = 50$ in Fig. 7 are similar to those for the low initial Reynolds number ($Re_0 = 6$, Fig. 6). The differences, however, between predicted quantities for a suspended and for a moving droplet are larger for $Re_0 = 50$. The evaporation constant for the suspended droplet is higher than that for the moving droplet during most of the droplet lifetime, as shown in Fig. 7d. This causes a much shorter droplet lifetime for the suspended droplet than the moving droplet. The steep increase in the evaporation constant for the moving droplet near the end of its lifetime is due to the formation of an envelope flame. This event can also be seen in Fig. 7a, where the slope in the $(d/d_0)^2$ plot becomes steeper for the moving droplet case. Despite that the moving droplet eventually develops an envelope flame, whereas the suspended droplet does not, the presence of the envelope flame at the very end of the moving droplet's life does not have an impact on its lifetime. In the absence of envelope flames, the difference in Reynolds number histories between the two cases is the only cause for their different vaporization rates. Note that the trend in Damköhler number is the same in Figs. 7c and 6c, namely, the Damköhler number increases for the moving droplet and decreases for the suspended droplet.

The combustion behavior for the two cases at $Re_0 = 8$ is quite different from the cases discussed earlier. Figure 8b compares the Reynolds number time histories between the suspended and the moving droplet case. Although the Reynolds number for the suspended droplet is again higher than that for the moving droplet throughout the droplet lifetime, the lifetime of the suspended droplet is approximately 30% longer than that of the moving droplet (Fig. 8a). Figure 8d shows that the evaporation constant for the moving droplet is higher than that for the suspended case during most of the droplet lifetime, despite that the suspended droplet experiences stronger convection than its counterpart. The difference in evaporation constants, which leads to the disparity in droplet lifetimes, is

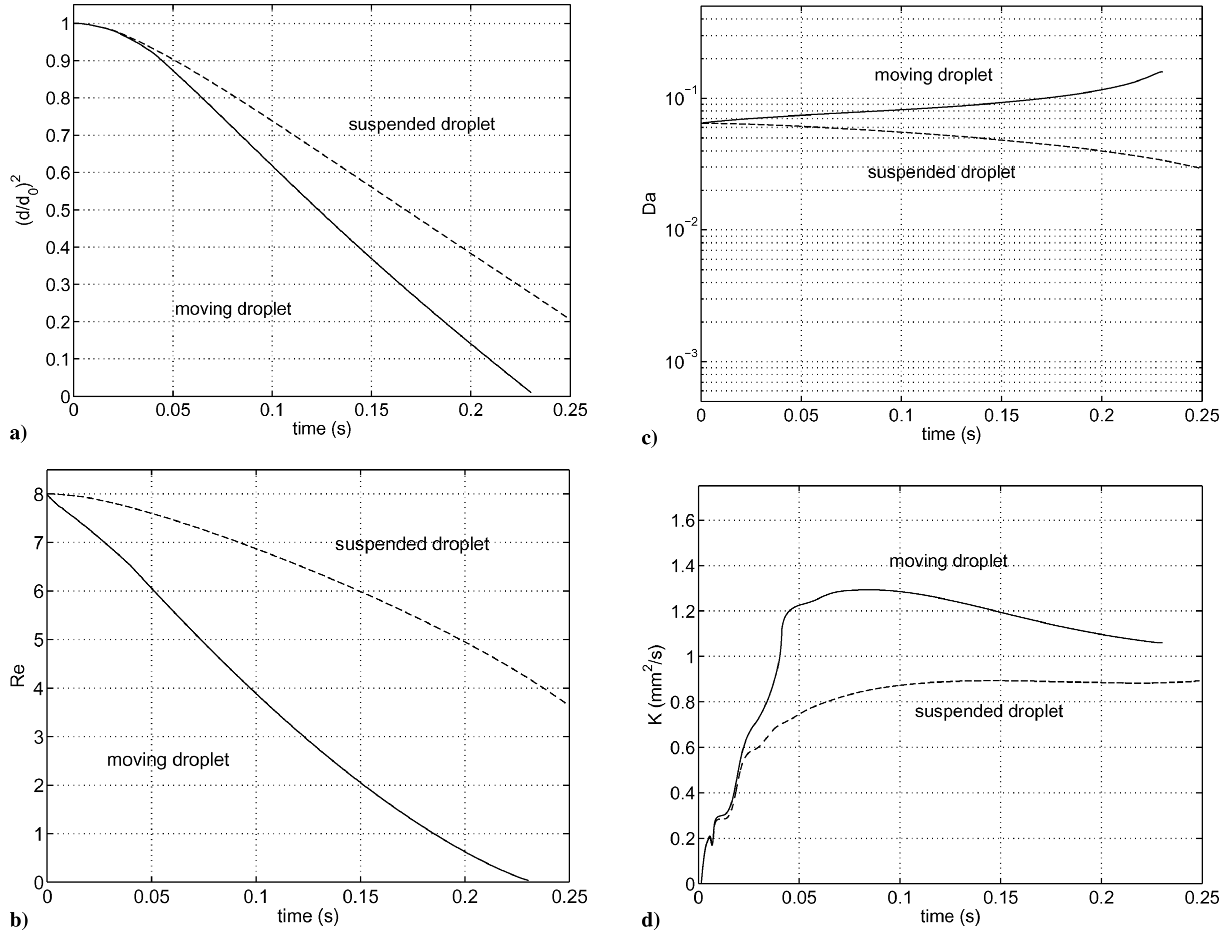

Fig. 8 Comparison between moving droplet and suspended droplet combustion for $Re_0 = 8$ ($d_0 = 500$ μm and $T_\infty = 1200$ K); time history of a) $(d/d_0)^2$, b) Reynolds number, c) Damköhler number, and d) K.

caused by the difference in flame configurations. The moving droplet develops an envelope flame at an early stage ($t = 40$ ms) of its lifetime. In contrast, the suspended droplet exhibits a transition flame during most of the droplet lifetime. The transition flame partially surrounds the droplet, but the temperature at the front of the droplet is the ambient temperature. (See Fig. 5c) Figure 8c shows that the Damköhler number increases with time for the moving droplet and decreases with time for the suspended droplet, which is the same trend noted for the other initial Reynolds numbers.

The results presented for the three different Reynolds numbers seem to suggest that a moving droplet tends to develop an envelope flame at some stage during its lifetime, whereas a suspended droplet develops an envelope flame only at low initial Reynolds numbers. The flame configurations present in a burning droplet are a function not only of the Reynolds number, but of the Damköhler number as well. Similar results were presented[31] using the kinetics of Westbrook and Dryer.[32] Although previous and current results are slightly different quantitatively, they remain qualitatively the same.

VI. Conclusions

The numerical results for n–heptane clearly indicate that, given the same initial conditions, suspended droplets and moving droplets can exhibit very different combustion behavior. The flame configurations present in a burning droplet are a function of both Reynolds and Damköhler number. For a moving droplet, the Reynolds number decreases with time, but the Damköhler number increases with time, whereas for a suspended droplet, the Reynolds and Damköhler number both decrease. The increasing Damköhler number associated with a moving droplet promotes the formation of an envelope flame at some point in the droplet lifetime. Over the range of initial Reynolds numbers considered (6, 8, and 50), a suspended droplet developed an envelope flame at only the lowest initial Reynolds number. The flame configurations present during droplet burning are of critical importance in determining the droplet lifetime.

Acknowledgments

This study was supported through U.S. Army Research Office Experimental Program to Simulate Research (EPSCoR) under Grant DAAD19-99-1-0116 and from NASA EPSCoR under Grant NCCS-572.

References

[1] Spalding, D. B., "Experiments on the Burning and Extinction of Liquid Fuel Spheres," *Fuel*, Vol. 32, 1953, pp. 169–185.

[2] Gollahalli, S. R., and Brzustowski, T. A., "The Effect of Pressure on the Flame Structure in the Wake of a Burning Hydrocarbon Droplet," *Proceedings of the Combustion Institute*, Vol. 15, 1975, pp. 409–417.

[3] Okajima, S., and Kumagai, S., "Experimental Studies on Combustion of Fuel Droplets in Flowing Air Under Zero- and High-Gravity Conditions," *Proceedings of the Combustion Institute*, Vol. 19, 1982, pp. 1021–1027.

[4] Nayagam, V., Hicks, M. C., Ackerman, M., Haggard, J. B., Jr., and Williams, F. A., "Droplet Combustion in a Slow Convective Flow," *Seventh International Microgravity Combustion Workshop*, NASA CP-2003-212376, 2003, pp. 157–160.

[5] Gokalp, I., Chauveau, C., Richard, J. R., Kramer, M., and Leuckel, W., "Observations on the Low Temperature Vaporization and Envelope or Wake Flame Burning of n-Heptane Droplets at Reduced Gravity," *Proceedings of the Combustion Institute*, Vol. 22, 1988, pp. 2027–2035.

[6] Dwyer, H. A., and Sanders, B. R., "Calculations of Unsteady Reacting Droplet Flows," *Proceedings of the Combustion Institute*, Vol. 22, 1988, pp. 1923–1929.

[7] Williams, F. A., Combustion Theory, 2nd ed., Benjamin/Cummings, Menlo Park, 1985, Chap. 1.

[8] Bird, R. B., Stewart, W. E., and Lightfoot, E. N., Transport Phenomena, Wiley, New York, 1960, pp. 567–572.

[9] Coffee, T. P., and Heimerl, J. M., "Transport Algorithms for Premixed, Laminar Steady-State Flames," *Combustion and Flame*, Vol. 43, 1981, pp. 273–289.

[10] Reid, R. C., Prausnitz, J. M., and Poling, B. E., The Properties of Gases and Liquids, McGraw–Hill, New York, 1987, Chaps. 7–11.

[11] Chung, T. H., Ajlan, M., Lee, L. L., and Starling, K. E., "Generalized Multiparameter Correlation for Nonpolar and Polar Fluid Transport Properties," *Industrial and Engineering Chemistry Research*, Vol. 27, No. 4, 1988, pp. 671–679.

[12] Wilke, C. R., "A Viscosity Equation for Gas Mixtures," *Journal of Chemical Physics*, Vol. 18, No. 4, 1950, pp. 517–519.

[13] McBride, B. J., Sanford, G., and Reno, M. A., "Coefficients for Calculating Thermodynamic and Transport Properties of Individual Species," NASA TM-4513, Oct. 1993.

[14] Hirschfelder, J. O., Curtiss, C. F., and Bird, R. B., *Molecular Theory of Gases and Liquids*, Wiley, New York, 1954, Chap. 8.

[15] Ramshaw, J. D., "Hydrodynamic Theory of Multicomponent Diffusion and Thermal Diffusion in Multitemperature Gas Mixtures," *Journal of Non-Equilibrium Thermodynamics*, Vol. 18, 1993, pp. 121–134.

[16] Haywood, R. J., Nafziger, R., and Renksizbulut, M., "A Detailed Examination of Gas and Liquid Phase Transient Processes in Convective Droplet Evaporation," *Journal of Heat Transfer*, Vol. 111, 1989, pp. 495–502.

[17] Pope, D. N., and Gogos, G., "Numerical Simulation of Fuel Droplet Extinction Due to Forced Convection," *Combustion and Flame* (to be published).

[18] Patankar, S. V., *Numerical Heat Transfer and Fluid Flow*, Hemisphere, Washington, D.C., 1980, Chaps. 2–7.

[19] VanDoormaal, J. P., and Raithby, G. D., "Enhancements of the SIMPLE Method for Predicting Incompressible Fluid Flows," *Numerical Heat Transfer*, Vol. 7, 1984, pp. 147–163.

[20] Peric, M., Kessler, R., and Scheuerer, G., "Comparison of Finite-Volume Numerical Methods with Staggered and Colocated Grids," *Computers and Fluids*, Vol. 16, No. 4, 1988, pp. 389–403.

[21] Vinokur, M., "On One-Dimensional Stretching Functions for Finite-Difference Calculations," *Journal of Computational Physics*, Vol. 50, 1983, pp. 215–234.

[22] Clift, R., Grace, J. R., and Weber, M. E., *Bubbles, Drops, and Particles*, Academic Press, New York, 1978, Chap. 5.

[23] Sayegh, N. N., and Gauvin, W. H., "Numerical Analysis of Variable Property Heat Transfer to a Single Sphere in High Temperature Surroundings," *AIChE Journal*, Vol. 25, No. 3, 1979, pp. 522–534.

[24] LeClair, B. P., Hamielec, A. E., Pruppacher, H. R., and Hall, W. D., "A Theoretical and Experimental Study of the Internal Circulation in Water Drops Falling at Terminal Velocity in Air," *Journal of the Atmospheric Sciences*, Vol. 29, 1972, pp. 728–740.

[25] Renksizbulut, M., and Yuen, M. C., "Numerical Study of Droplet Evaporation in a High-Temperature Stream," *Journal of Heat Transfer*, Vol. 105, 1983, pp. 389–397.

[26] Renksizbulut, M., and Yuen, M. C., "Experimental Study of Droplet Evaporation in a High-Temperature Air Stream," *Journal of Heat Transfer*, Vol. 105, 1983, pp. 384–388.

[27] Kumagai, S., Sakai, T., and Okajima, S., "Combustion of Free Fuel Droplets in a Freely Falling Chamber," *Proceedings of the Combustion Institute*, Vol. 13, 1971, pp. 779–785.

[28] Jackson, G. S., Avedisian, C. T., and Yang, J. C., "Observations of Soot During Droplet Combustion at Low Gravity: Heptane and Heptane/Monochloroalkane Mixtures," *International Journal of Heat and Mass Transfer*, Vol. 35, No. 8, 1992, pp. 2017–2033.

[29] Lee, K. O., Manzello, S. L., and Choi, M. Y., "The Effects of Initial Diameter on Sooting and Burning Behavior of Isolated Droplets Under Microgravity Conditions," *Combustion Science and Technology*, Vol. 132, 1998, pp. 139–156.

[30] Marchese, A. J., Dryer, F. L., and Nayagam, V., "Numerical Modeling of Isolated n-Alkane Droplet Flames: Initial Comparisons with Ground and Space-Based Microgravity Experiments," *Combustion and Flame*, Vol. 116, 1999, pp. 432–459.

[31] Pope, D. N., Lu, K., and Gogos, G., "Combustion of Moving Droplets and of Droplets Suspended within a Convective Environment: Transient Numerical Results," *Proceedings of the Third Joint Meeting of the U.S. Sections of The Combustion Institute*, Combustion Inst., Pittsburgh, PA, 2003; also Paper E15, pp. 1–6.

[32] Westbrook, C. K., and Dryer, F. L., "Simplified Reaction Mechanisms for the Oxidation of Hydrocarbon Fuels in Flames," *Combustion Science and Technology*, Vol. 27, 1981, pp. 31–43.